

X-ray modelling of galaxy cluster gas and mass profiles

Alastair J. R. Sanderson[★] and Trevor J. Ponman

School of Physics and Astronomy, University of Birmingham, Edgbaston, Birmingham B15 2TT

Accepted 2009 October 15. Received 2009 September 15

ABSTRACT

We present a parametric analysis of the intracluster medium and gravitating mass distribution of a statistical sample of 20 galaxy clusters using the phenomenological cluster model of Ascasibar and Diego. We describe an effective scheme for the estimation of errors on model parameters and derived quantities using bootstrap resampling. We find that the model provides a good description of the data in all cases and we quantify the mean fractional intrinsic scatter about the best-fitting density and temperature profiles, finding this to have median values across the sample of 2 and 5 per cent, respectively. In addition, we demonstrate good agreement between r_{500} determined directly from the model and that estimated from a core-excluded global spectrum. We compare cool core and non-cool core clusters in terms of the logarithmic slopes of their gas density and temperature profiles and the distribution of model parameters and conclude that the two categories are clearly separable. In particular, we confirm the effectiveness of the logarithmic gradient of the gas density profile measured at $0.04r_{500}$ in differentiating between the two types of cluster.

Key words: methods: data analysis – galaxies: clusters: general – cooling flows – X-rays: galaxies: clusters.

1 INTRODUCTION

Given the dominance of gravity in the Universe, the masses of large-scale structures such as clusters of galaxies are of great importance in cosmological modelling (e.g. Press & Schechter 1974) as well as in astrophysical interpretation of their properties. The main methods for measuring cluster masses directly are by gravitational lensing, virial analysis of the galaxy velocity distribution and X-ray mapping of the pressure profile of the hot intracluster medium (ICM; e.g. see the review by Voit 2005 and references therein).

Using X-ray observations to measure cluster masses has the advantage that clusters present a sharp contrast against the X-ray background (which is itself relatively faint and uniform on cluster angular scales), since their (mainly bremsstrahlung) emissivity scales with $\rho_{\text{gas}}^2 \sqrt{T}$, and the ICM is compressed and strongly heated in clusters, raising both these quantities by large factors. Moreover, a number of studies based on cosmological simulations have validated the crucial assumption of hydrostatic equilibrium (HSE) in the X-ray modelling of clusters, quantifying the systematic bias caused by non-thermal pressure support in the range of ~ 5 –20 per cent, depending on the dynamical state (Evrard, Metzler & Navarro 1996; Rasia et al. 2006; Nagai, Vikhlinin & Kravtsov 2007; Piffaretti & Valdarnini 2008; Lau, Kravtsov & Nagai 2009).

However, measuring X-ray cluster masses directly can be challenging and typically requires high-quality observations, restricting

the number of objects for which reliable masses can be obtained and typically favouring the most massive and/or luminous clusters. The usual approach is to model the (deprojected) gas temperature, $T(r)$, and density, $\rho(r)$, separately and combine them to infer the mass profile under the assumption of HSE, via the following equation:

$$M_{\text{grav}}(r) = -\frac{kT(r)r}{G\mu m_p} \left[\frac{d \ln \rho}{d \ln r} + \frac{d \ln T}{d \ln r} \right] \quad (1)$$

(e.g. Fabricant, Lecar & Gorenstein 1980), where μ is the mean molecular weight of the gas and m_p is the proton mass. Alternatively, the pressure gradient can be estimated directly and combined with the density to calculate the mass (e.g. Voigt & Fabian 2006). The resulting values can then be separately fitted with a mass model such as the NFW profile (Navarro, Frenk & White 1995). This approach treats the density and temperature (or pressure) separately, and thus does not exploit the natural coupling between these quantities that is implied by the assumption of HSE in a well-behaved gravitational potential. Moreover, the inferred mass distribution can have negative values, particularly if the gas profiles are insufficiently smooth.

Another method is to use a model for the total mass density and either a parametric (e.g. Lloyd-Davies, Ponman & Canon 2000) or non-parametric (e.g. Allen 1998; Schmidt & Allen 2007) form for the gas density to predict $T(r)$ (assuming HSE), which is then fitted to the observed data. However, this method can yield unphysical behaviour in the form of negative temperatures.

Recently, Ascasibar & Diego (2008, hereafter AD08) have developed a simple, phenomenological cluster model, based on the Hernquist (1990) mass profile, which avoids unphysical behaviour

[★]E-mail: ajrs@star.sr.bham.ac.uk

and provides a full description of the gas and mass distributions with only five adjustable parameters. The model can be simultaneously fitted to both the gas temperature and density profiles, providing additional stability and enabling it to be applied to even relatively poor quality data. In this paper, we assess the performance of this model as applied to a statistical sample of clusters – that of Sanderson, Ponman & O’Sullivan (2006) and Sanderson, O’Sullivan & Ponman (2009a, hereafter SOP09), which incorporates both cool core (CC) and non-CC clusters. We investigate the effectiveness of the model through analysis of the residuals from the best fit and explore some of its capabilities in measuring derived cluster properties.

Throughout this paper, we adopt the following cosmological parameters: $H_0 = 70 \text{ km s}^{-1} \text{ Mpc}^{-1}$, $\Omega_m = 0.3$ and $\Omega_\Lambda = 0.7$. All errors are 1σ , unless otherwise stated.

2 CLUSTER SAMPLE

The objects studied in this paper comprise the statistical sample of 20 galaxy clusters observed with *Chandra* presented in Sanderson et al. (2006) and SOP09, where details of the selection and the basic properties of this sample can be found. Briefly, it consists of 20 clusters drawn from the flux-limited catalogue of Ikebe et al. (2002), excluding the Coma, Fornax and Centaurus clusters, owing to their very large angular sizes. It is interesting to note that, while half of the sample show some indication of merging activity (Sanderson et al. 2006), there are no seriously disturbed clusters of the type that would prevent a one-dimensional radial analysis, unlike the two (out of 33) highly irregular clusters present in the representative *XMM-Newton* cluster structure survey (REXCESS, e.g. Böhringer et al. 2007; Croston et al. 2008).

2.1 Spectral profiles and errors

Deprojected gas temperature and density profiles were obtained in discrete annular bins as described in SOP09, but an improved method was used here to evaluate errors on these quantities, given the large interdependence between radial bins in the `PROJECT` scheme in `XSPEC`. A series of 200 Poisson realizations of the best-fitting `PROJECT` model were generated, using the same background and response files, to produce a series of simulated source spectra. Each set of annular spectra was then fitted with the `PROJECT` model and treated like the original data, using the same corresponding background spectra and response files. This produced a suite of simulated measurements of gas temperature and density in each annulus, which were used to evaluate the error in each radial bin using the median absolute deviation (MAD) of the values, which is a robust estimator of the standard deviation. The MAD is particularly well suited to heavy-tailed distributions, although it is less efficient when applied to Gaussian ones (e.g. see Beers, Flynn & Gebhardt 1990, for a discussion).

3 CLUSTER MODEL

We use the phenomenological cluster model of AD08, which describes the gas density and temperature profile in a state of HSE in a Hernquist (1990) gravitational potential with just five free parameters. The model assumes a polytropic ICM, with central gas temperature, T_0 , modified by a variable CC component controlled by the parameter t ($0 < t < 1$), which becomes important inside a radius a fraction α ($0 < \alpha < 1$) times the dark matter scale radius, a . The gas density normalization is expressed in terms of a fraction, f , of the cosmic mean baryon fraction. The model yields smoothly

varying profiles which avoid unphysical behaviour, such as negative values, while capturing the typically observed cluster properties with good accuracy – e.g. the single-peaked gas temperature profile commonly found in CC clusters.

The use of a Hernquist (1990) parametrization for the mass profile has the advantage of yielding a convergent projected distribution (since the mass density falls off at large radii as r^{-4}), unlike the Navarro et al. (1995) profile, for example. This property enables direct comparison of projected X-ray masses derived from the model with those measured using gravitational lensing within a fixed aperture. Such a comparison is presented in Richard et al. (2009), based on the AD08 model analysis of Sanderson, Edge & Smith (2009b), and reveals generally good agreement between the X-ray and strong gravitational lensing projected masses within a cylinder of a radius of 250 kpc, particularly for clusters without evidence of significant dynamical disturbance.

3.1 Model fitting

The cluster model is fitted simultaneously to the observed temperature and density profiles and the χ^2 statistic is evaluated and minimized for both data sets combined. This joint fit introduces extra stability into the minimization and provides tighter constraints on the model parameters, exploiting the coupling between the gas density and temperature implied by the assumption of HSE.

Asymmetric errors on $T(r)$ and $\rho_{\text{gas}}(r)$ are handled by using the upper measurement error when the model lies above the measured value and the lower measurement error otherwise. Since the model is not expected to perform well on small scales (e.g. see AD08), where the effects of stellar baryonic mass become non-negligible, data points within 5 kpc are excluded from the fit. In the case of 2A 0335+096 and Abell 262, larger exclusion radii were used, of 20 and 8 kpc, respectively, within which a clear deviation of the data from the model was evident, associated with a departure from HSE as a result of disruptions in the cores of these clusters (Mazzotta, Edge & Markevitch 2003; Clarke et al. 2009). The best-fitting model parameters and 1σ errors are listed in Table 1.

3.2 Error estimates

One of the main challenges in modelling cluster properties is the process of deriving error estimates, on both the parameters of the model itself and on any derived quantity evaluated using those parameters. Errors are particularly important when fitting scaling relations with weighted regression techniques and when attempting to determine intrinsic scatter in the measurement of some quantity over and above the purely statistical dispersion. Although there are many reliable ways of determining error estimates for fitted model parameters, these do not provide errors directly on *derived* quantities, which are usually desirable in a cluster modelling analysis (e.g. measuring r_{500} , or the gas fraction within this radius).

In this situation, a common approach is to generate a set of Monte Carlo (MC) realizations of the original data, which can be used to produce a corresponding set of best-fitting models. Errors on any parameter of the model or derived quantity are then determined from the spread in values obtained, typically measured using the standard deviation. However, the success of this method depends critically on the prescription used to generate the MC realizations, which must produce realistic mock data sets that capture the essential properties of the original measurements.

Often what is done is simply to perturb the observed data, using the measured value as the mean for a Gaussian random number

Table 1. Best-fitting model parameters for each cluster and corresponding r_{500} , listed in order of increasing mean temperature as measured in SOP09. Errors are 1σ , estimated from 200 bootstrap resamples. The CC status is as determined in Sanderson et al. (2006).

Name	Mean kT (keV)	T_0 (keV)	t	α (kpc)	α	f	r_{500} (kpc)	CC status
NGC 5044	$1.17^{+0.04}_{-0.05}$	3.40 ± 2.08	0.17 ± 0.08	404 ± 285	0.37 ± 0.14	0.01 ± 0.02	717 ± 254	CC
Abell 262	$2.08^{+0.11}_{-0.09}$	2.74 ± 0.18	0.21 ± 0.12	333 ± 53	0.05 ± 0.02	0.52 ± 0.13	634 ± 27	CC
Abell 1060	$2.92^{+0.11}_{-0.11}$	4.42 ± 0.10	0.73 ± 0.03	314 ± 19	0.10 ± 0.07	0.38 ± 0.04	770 ± 14	Non-CC
Abell 4038	$3.04^{+0.07}_{-0.09}$	4.66 ± 0.08	0.52 ± 0.06	349 ± 14	0.09 ± 0.02	0.54 ± 0.05	796 ± 6	Non-CC
Abell 1367	$3.22^{+0.18}_{-0.18}$	3.84 ± 0.30	0.76 ± 0.32	1200 ± 659	0.03 ± 0.13	2.35 ± 1.66	768 ± 59	Non-CC
Abell 2147	$3.69^{+0.18}_{-0.18}$	5.88 ± 0.54	0.71 ± 0.09	1007 ± 143	0.52 ± 0.72	0.45 ± 0.37	968 ± 44	Non-CC
2A 0335+096	$4.09^{+0.13}_{-0.13}$	6.53 ± 0.36	0.00 ± 0.02	648 ± 67	0.10 ± 0.01	0.47 ± 0.04	998 ± 34	CC
Abell 2199	$4.50^{+0.20}_{-0.24}$	7.01 ± 0.43	0.16 ± 0.03	605 ± 124	0.08 ± 0.02	0.63 ± 0.09	1025 ± 47	CC
Abell 496	$4.80^{+0.15}_{-0.14}$	7.26 ± 1.70	0.17 ± 0.03	769 ± 339	0.15 ± 0.05	0.32 ± 0.17	1064 ± 152	CC
Abell 1795	$5.62^{+0.36}_{-0.35}$	9.41 ± 0.86	0.18 ± 0.04	1032 ± 273	0.16 ± 0.02	0.50 ± 0.08	1206 ± 56	CC
Abell 3571	$6.41^{+0.23}_{-0.23}$	9.51 ± 0.18	0.21 ± 0.21	501 ± 24	0.02 ± 0.01	0.83 ± 0.05	1134 ± 15	Non-CC
Abell 2256	$6.52^{+0.39}_{-0.36}$	17.27 ± 5.36	0.35 ± 0.11	4176 ± 1717	0.75 ± 0.30	0.06 ± 0.03	1433 ± 100	Non-CC
Abell 85	$6.64^{+0.20}_{-0.20}$	8.94 ± 0.58	0.14 ± 0.03	825 ± 121	0.08 ± 0.02	0.85 ± 0.15	1164 ± 41	CC
Abell 3558	$7.17^{+0.49}_{-0.46}$	9.60 ± 0.65	0.45 ± 0.14	879 ± 157	0.11 ± 0.06	0.72 ± 0.26	1214 ± 44	Non-CC
Abell 3667	$7.60^{+0.38}_{-0.37}$	11.88 ± 0.66	0.40 ± 0.07	2374 ± 339	0.11 ± 0.05	1.38 ± 0.54	1305 ± 54	Non-CC
Abell 478	$8.23^{+0.26}_{-0.26}$	12.57 ± 0.76	0.14 ± 0.03	886 ± 174	0.12 ± 0.01	0.74 ± 0.09	1351 ± 49	CC
Abell 3266	$8.38^{+0.67}_{-0.43}$	11.56 ± 0.56	0.00 ± 0.21	1290 ± 135	0.02 ± 0.01	1.23 ± 0.15	1345 ± 32	Non-CC
Abell 2029	$8.96^{+0.30}_{-0.30}$	12.29 ± 1.49	0.21 ± 0.02	785 ± 207	0.13 ± 0.03	0.60 ± 0.13	1327 ± 104	CC
Abell 401	$9.16^{+1.41}_{-1.06}$	12.43 ± 0.86	0.66 ± 0.23	964 ± 190	0.15 ± 0.14	0.94 ± 0.17	1362 ± 63	Non-CC
Abell 2142	$9.50^{+0.43}_{-0.42}$	16.97 ± 1.14	0.35 ± 0.03	1248 ± 164	0.21 ± 0.04	0.50 ± 0.11	1591 ± 63	Non-CC

generator, with the measurement error as the standard deviation. However, this method has two drawbacks. First, the measured values already include some random noise and thus are imperfect estimates of the expectation value for the distribution at the radius of the measurement. For example, in the case of an extreme outlier, all MC realizations based on this value would automatically ‘start’ at an extreme point compared to the underlying distribution that generated the data point (and compared to which it was judged to be an outlier), thus biasing them significantly. This problem could be mitigated by using the predicted value from the best-fitting model as the mean for the Gaussian random perturbation.

The second problem with the above approach is that it assumes that the data points are Gaussian-distributed about the best fit with a dispersion given by the measurement errors alone. No allowance is made for intrinsic scatter in the data, which is a common situation in astronomical analyses. For example, in the case of modelling galaxy clusters, the frequent assumption of spherical or even ellipsoidal geometry will always be violated at some level as a result of substructures and other features, which add scatter to azimuthal profiles in addition to that from measurement uncertainties. Therefore, to avoid both these problems we use bootstrap resampling to generate a set of realizations of the observed data.

3.3 Bootstrap resampling

A set of N realizations of the original data were generated by separate bootstrap resampling of the temperature and density data, with $N = 200$. The cluster model was then fitted to each realization data set, treating it identically to the original data, to produce a series of N values of the model parameters. In calculating derived quantities, such as r_{500} , the quantity was evaluated separately for each bootstrap realization, to yield N values. The uncertainty on any given quantity was then obtained from the spread in the bootstrapped values,

as measured using the MAD, as described in Section 2.1. In a few cases, where the best fit and many of the bootstrap values were at the lower limit of the parameter (e.g. $t = 0$ for 2A 0335+096 and Abell 3266; see Table 1), the MAD produced unrealistically low errors. In these cases we calculated the error using the interquartile range of the N bootstrap realizations, adjusted for a normally consistent estimate of the standard deviation by dividing by $2 \times \text{qnorm}(3/4)$ (≈ 1.35), where qnorm is the normal quantile distribution. This was done wherever the MAD was less than half the adjusted interquartile range (IQR) value.

4 TESTING THE MODEL

The left-hand panel of Fig. 1 shows the residuals from the model for both the gas temperature and density, as a function of scaled radius. There is no indication of any significant systematic trends with radius and the marginal distribution of the residuals is consistent with the Gaussian distribution expected from the measurement errors alone, apart from a slight excess of positive temperature residuals (as also seen in Sanderson et al. 2009b). Note that the gas density profiles extend only to the penultimate spectral bin, owing to the non-trivial volume element associated with the outermost annulus in the deprojection (Sanderson et al. 2006).

To assess the reliability of the cluster model, we have compared the predicted r_{500} values for each cluster with those obtained from an independent method in SOP09, based on a single spectral fit. Briefly, the r_{500} values from SOP09 were determined iteratively by extracting a spectrum in the range of $0.15\text{--}0.2r_{500}$, fitting an APEC hot plasma model to it and determining r_{500} from the resulting temperature, based on the $M\text{--}T_X$ relation of Vikhlinin et al. (2006), adjusted for the effect of using a different aperture. The right-hand panel of Fig. 1 shows the comparison of r_{500} obtained with the two methods, and it is clear that there is generally very good agreement.

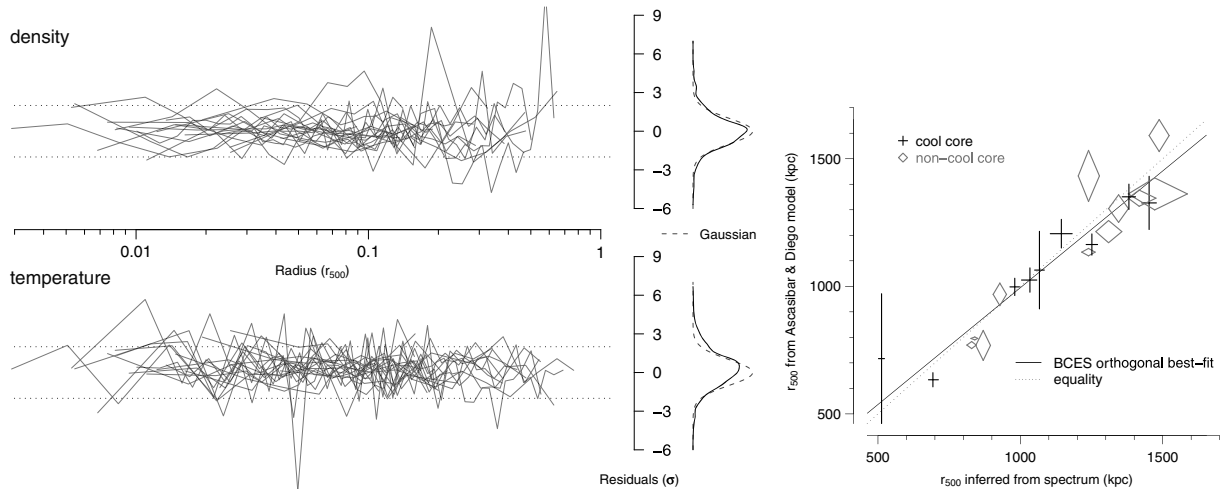


Figure 1. *Left:* a comparison of the residuals from the best-fitting AD08 model, normalized by the measurement errors on each point, as a function of scaled radius for both the gas density and temperature data. Each line represents a different cluster and shows the fluctuations about the model purely in terms of the statistical errors on the observed data points. Dotted lines mark $\pm 2\sigma$, and the marginal distribution of the data is depicted as a kernel-smoothed density estimate, compared to a Gaussian of unit variance. *Right:* the comparison between r_{500} calculated from the cluster model and from the mean temperature estimated in SOP09. The solid line is the best-fitting BCES-weighted orthogonal regression, with a slope of 0.91 ± 0.11 , and the dotted line is the locus of equality.

A weighted orthogonal linear regression using the bivariate correlated errors and intrinsic scatter (BCES) method of Akritas & Bershady (1996) yields a best-fitting slope of 0.91 ± 0.11 , using a pivot point set at the mean of all the X and Y values, so as to decouple the measurement errors on the slope and intercept as far as possible. The corresponding best-fitting intercept is -15 ± 20 , which is fully consistent with a zero offset between the two methods.

4.1 Residual real variance about the best fit

Although the model appears to be a good representation of the data, departures from the fit are expected, since real clusters are not perfectly spherical or fully in HSE. Such deviations can be quantified in terms of the real variance of the data about the model, beyond that expected from the measurement errors, i.e. the intrinsic scatter. As described in Appendix A, we calculate the mean fractional intrinsic scatter about the best-fitting gas temperature and density profiles using equations (A2) and (A3). The left-hand panel of Fig. 2 shows the mean values of the intrinsic scatter in gas density and temperature as a dot plot, with the clusters listed in order of decreasing scatter in density from top to bottom, which is below 10 per cent in all cases. The median values across the sample are 0.023 and 0.048 for the density and temperature, respectively.

It can be seen from Fig. 2 that the non-CC clusters have a broadly similar mean fractional intrinsic scatter in both temperature and density, whereas most of the CC clusters have quite high scatter in temperature. This is caused by instabilities in the deprojection, possibly as a result of non-spherical geometry or multiphase gas (Fabian et al. 2006), which result in oscillations in the temperature profile recovered using the `XSPEC PROJECT` model (Russell, Sanders & Fabian 2008). Nevertheless, it is clear from Fig. 1 that any such fluctuations are small compared to the measurement errors and that the model performs well in describing the data. Furthermore, this noise can easily be smoothed to clearly reveal the underlying trend (Sanderson et al. 2006).

The impact of oscillatory fluctuations on the intrinsic scatter can be gauged by rebinning the original profiles, grouping pairs of bins together and recalculating the mean fractional intrinsic scat-

ter about the original best-fitting profiles. The error in each new bin is calculated by adding in quadrature the errors on the constituent bins and a characteristic radius is assigned based on the inner- and outermost bounding radii of the constituent bins, as per Sanderson et al. (2006). This process will suppress oscillatory behaviour, which causes neighbouring bins to be anticorrelated, but will not significantly alter any other systematic deviations. The corresponding dot plot for the rebinned profiles is plotted in the right-hand panel of Fig. 2 and it can be seen that the fractional scatter in the temperature is reduced markedly for the CC clusters, while the density scatter is mostly unaffected. In particular, the cluster ranking by density scatter is largely preserved. This demonstrates that the intrinsic scatter in density is more representative of bulk systematic deviations from the model, whereas oscillatory deprojection instabilities can contribute significantly to the temperature scatter, particularly for CC clusters.

Such instabilities in the deprojection are mainly confined to the CC itself, where the temperature gradient is steep (e.g. Sanderson et al. 2006). This can be seen in Fig. 3, which shows a significant correlation between the scatter in temperature (from the original profiles) and the logarithmic slope of the gas temperature profile at $0.04r_{500}$ (see Section 5.1), demonstrating that the clusters with the largest intrinsic scatter all have steep core temperature gradients. The only exception is also the only galaxy group in the sample (NGC 5044). Such cool objects radiate predominantly line emission which provides much tighter constraints on the temperature than the slope of the bremsstrahlung continuum, since line ratios are very sensitive to temperature. This property enables a cleaner separation of the different temperature components projected on to inner annuli from hotter outer shells in CC dominated by line emission (i.e. $kT \lesssim 2$ keV), and results in smoother profiles and less intrinsic scatter about the best-fitting model.

Notwithstanding the impact of deprojection oscillations on the temperature profile, it is apparent that the mean fractional intrinsic scatter in the gas density serves to quantify the extent to which the model provides a good description of the data. For example, three of the four clusters with mean fractional intrinsic scatter in the density exceeding 5 per cent are known merging systems: Abell 3667

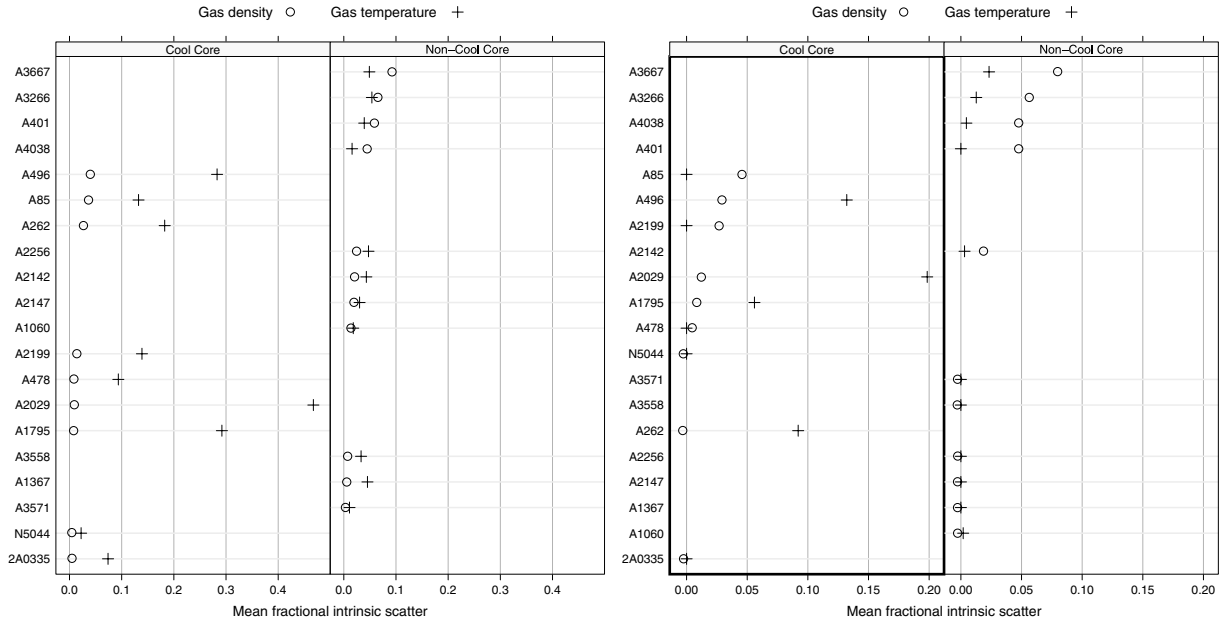


Figure 2. Dot plots of the mean fractional intrinsic scatter about the best-fitting model for each cluster, in both the gas density and temperature for the original (left-hand panel) and rebinned (right-hand panel) profiles. In each panel, the clusters are arranged in order of decreasing scatter in density from top to bottom and are separated according to their CC status.

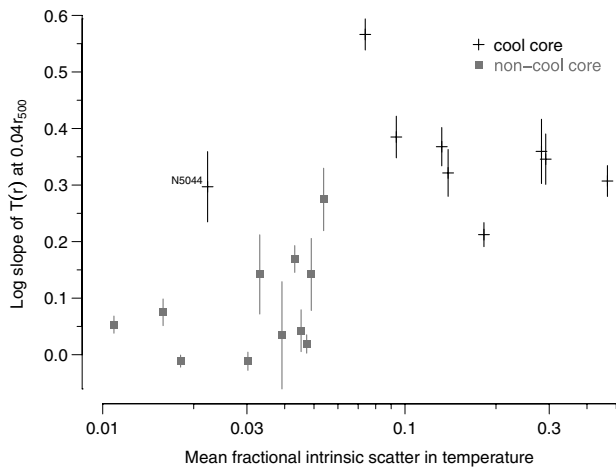


Figure 3. The relationship between the mean fractional intrinsic scatter from the model in temperature and the logarithmic slope of the temperature profile at $0.04r_{500}$, with the outlier galaxy group NGC 5044 labelled (see text for details).

(e.g. Owers, Couch & Nulsen 2009), Abell 3266 (e.g. Finoguenov et al. 2006) and Abell 401 (e.g. Sakelliou & Ponman 2004). Such objects are known to have somewhat distorted morphologies and may not be in HSE. Nevertheless, even Abell 3667 – the cluster with the largest intrinsic scatter – has a reasonably regular morphology that justifies the assumption of azimuthal symmetry (see e.g. the X-ray/optical overlay image in fig. 12 of Owers et al. 2009). Furthermore, all but three of our sample (Abell 2147, 2A 0335+096 and NGC 5044) were analysed by Mohr, Mathieson & Evrard (1999), who used either single or double β -model fits to *ROSAT* images in order to estimate gas and total masses, finding a reasonable match to the data in all cases.

5 RESULTS

5.1 Gas profile gradients

A particularly attractive feature of well-behaved and smoothly varying analytic models, such as that of AD08, is the ability to evaluate the gradient of predicted quantities at arbitrary radii. For example, the gradients of the temperature and density profiles are particularly sensitive indicators of central cooling, which causes a progressive steepening in both cases (e.g. Ettori & Brighenti 2008). Fig. 4 shows profiles of the gas density gradient as a function of scaled radius for the model fits. It can be seen that inside $0.05r_{500}$ the CC log

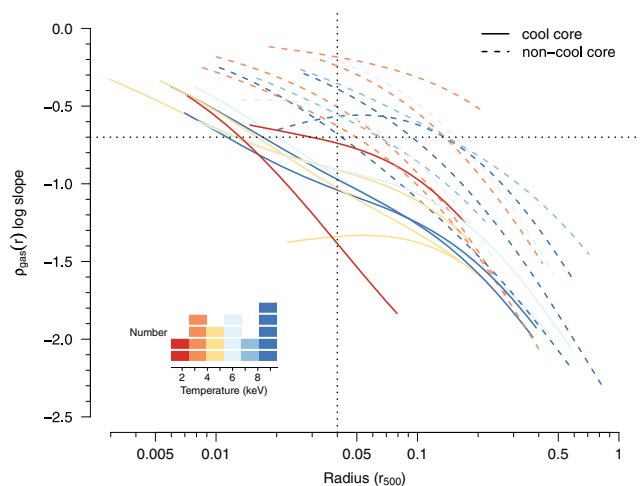


Figure 4. Logarithmic slope of the gas density profile as a function of scaled radius, coloured according to the mean cluster temperature, depicted by the inset histogram. Curves are plotted within the radial range used to fit the model. The dotted lines indicate a value of -0.7 at $0.04r_{500}$, which corresponds to the value of this parameter which Vikhlinin et al. (2007) used to identify strong cooling flow clusters (see also Sanderson et al. 2009b).

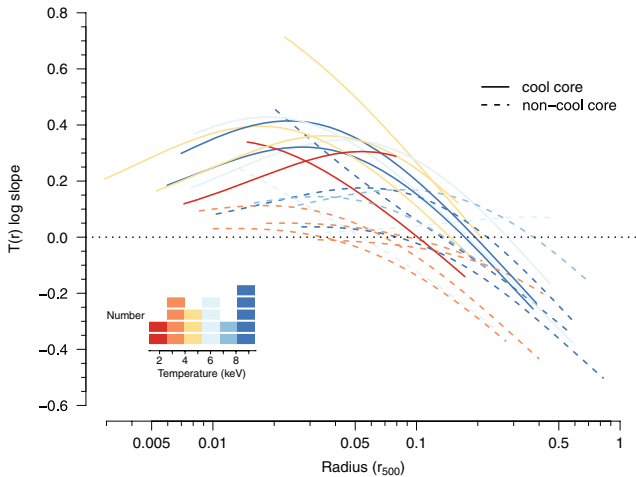


Figure 5. Logarithmic slope of the gas temperature profile as a function of scaled radius, coloured according to the mean cluster temperature, depicted by the inset histogram. Curves are plotted within the radial range used to fit the model. Intersection of the curves with the dotted zero line identifies the radius of the peak temperature.

gradients are steeper (i.e. more negative) than those of the non-CC clusters, and in the case of 2A 0335+096 they appear consistent with a pure power law (i.e. constant log gradient); otherwise all clusters show gradual flattening of the density profile (log gradient profiles approaching zero).

Towards the outskirts ($\gtrsim 0.3r_{500}$), $\rho_{\text{gas}}(r)$ steepens progressively with radius compared to a standard isothermal β -model, as originally discovered by Vikhlinin, Forman & Jones (1999). The shape and normalization of the profiles in Fig. 4 are consistent with the recent findings of Croston et al. (2008), based on *XMM-Newton* observations of a representative cluster sample, but are able to reach smaller radii, owing to the better spatial resolution of *Chandra*.

The bifurcation between CC and non-CC clusters in Fig. 4 motivates the use of the surface brightness ‘cuspsiness’ as an effective proxy for CC status (Vikhlinin et al. 2007; Ettori & Brighenti 2008; Sanderson et al. 2009b). In particular, Vikhlinin et al. identified the logarithmic gradient of the gas density profile at $0.04r_{500}$ as a proxy for the strength of cooling (see also Sanderson et al. 2009b), which is indicated by the vertical dotted line in Fig. 4: a value of -0.7 cleanly separates the two categories of cluster.

The equivalent plot of the logarithmic gradient of the gas temperature profile is shown in Fig. 5. Once again it can be seen that, within $0.05r_{500}$, the CC clusters all have steeper (in this case, positive) gradients – the only exception is the merging, non-CC cluster Abell 3266 (the only dashed line in Fig. 5 exceeding a logarithmic slope of 0.3). Choosing $0.04r_{500}$ as a fiducial radius, the relationship between the logarithmic gradient of the gas temperature and density profiles is plotted in Fig. 6, clearly revealing the separation between the CC and non-CC clusters (cf. SOP09). The most obvious outlier is the CC poor cluster Abell 262, which appears to lie closer to the non-CC points. This cluster unquestionably hosts a CC (e.g. see the temperature profile in Sanderson et al. 2006), but its inner core has been disrupted by repeated active galactic nuclei (AGN) outbursts occurring on the scale of $0.04r_{500}$ (25 kpc; e.g. Clarke et al. 2009), which could flatten the temperature and density gradients as observed.

It is apparent from Fig. 5 that all the non-CC curves intersect the zero line, implying that their temperature profiles turn over at least slightly at small radii; indeed, this can be seen from the projected

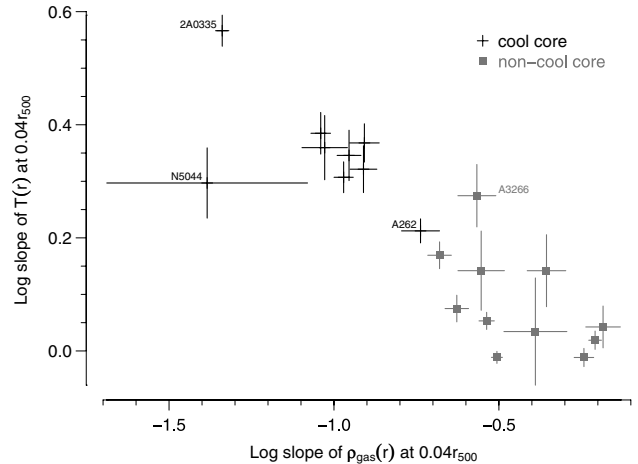


Figure 6. The relationship between the logarithmic slopes of the gas temperature and density profiles evaluated at $0.04r_{500}$, with obvious outliers identified.

temperature profiles plotted in fig. 3 of Sanderson et al. (2006), as well as the fact that the values of the AD08 normalized central temperature parameter, t , lie below unity (which would correspond to a pure polytropic profile) in all cases (Table 1). Nevertheless, with the exception of Abell 3266 (where the impact of merger-induced deviations from HSE may be affecting the model fit), the effect is small and does not manifest itself in the logarithmic slopes of the gas density profile (Fig. 4).

5.2 Cool core versus non-cool core clusters

With a parametric analysis of a statistical sample we are able to address the variation in cluster structure and, in particular, the comparison between clusters with and without a CC. In Fig. 7 we explore the relationships between the model parameters using a parallel coordinates plot, separating the CC and non-CC clusters. This is a tool for hyperdimensional data visualization (e.g. Wegman 1990),

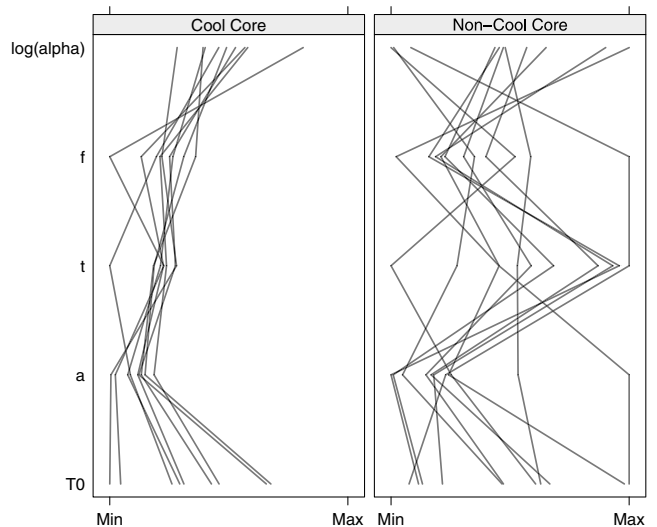


Figure 7. A parallel coordinates plot of the cluster model parameters, comparing CC and non-CC core clusters. Each line represents a different cluster and links together its values for each parameter (see text for details). Note that the AD08 model α parameter has been logged for display purposes.

which is implemented in the `LATTICE` package in R^1 (Sarkar 2008). A series of variables (in this case the values of the best-fitting model parameters) are plotted in a one-dimensional form along a common horizontal axis spanning the range of the data in each case. These univariate plots are arranged vertically and lines are drawn linking points for the same cluster between all the variables.

It is clear from Fig. 7 that the CC cluster lines are more tightly bunched compared to the non-CC clusters, demonstrating that CC clusters have more uniform properties, possibly reflecting a more diverse history for non-CC clusters. This could be because the formation of a CC only takes place in more relaxed clusters, which therefore exhibit greater uniformity or could be the result of a dynamical disturbance inhibiting or disrupting the formation of a CC (cf. Sanderson et al. 2009b). A much larger (but still representative) cluster sample would be required to clarify these trends. Furthermore, this systematic variation in structure between CC and non-CC clusters is something that cosmological simulations should be able to reproduce.

6 DISCUSSION AND CONCLUSIONS

We have demonstrated that the AD08 cluster model is well suited to parametrizing the gas and mass distributions of a wide range of galaxy clusters. The model is stable and easy to fit, and it performs well with even sparse and noisy data (as few as four radial bins). It also has the advantage of avoiding unphysical behaviour (i.e. negative values) and, being based on the Hernquist (1990) profile, yields convergent projected masses, facilitating easy comparison with gravitational lensing measurements (e.g. Richard et al. 2009). The use of bootstrap resampling of the input gas temperature and density profile data allows error estimates to be made directly on model parameters and any derived quantity.

The fact that the model can be successfully applied to relatively poor quality data greatly increases the number of clusters for which a full X-ray mass analysis is possible, enabling better calibration of mass proxies and scaling relations for cosmological studies. Furthermore, the ability to easily determine important diagnostics of cluster physics directly from the model is of great benefit to studies of galaxy feedback and cluster evolution (e.g. Sanderson et al. 2009b). For example, the use of a simple cluster modelling analysis like this is potentially a powerful tool for exploring the effectiveness of baryon physics implementations in cosmological simulations, by probing structural variations within synthetic cluster populations and comparing them with real clusters.

ACKNOWLEDGMENTS

AJRS acknowledges support from the Science and Technology Facilities Council (STFC). This work has made extensive use of the `R` software package.

REFERENCES

- Akritas M. G., Bershady M. A., 1996, *ApJ*, 470, 706
 Allen S. W., 1998, *MNRAS*, 296, 392
 Ascibar Y., Diego J. M., 2008, *MNRAS*, 383, 369 (AD08)
 Beers T. C., Flynn K., Gebhardt K., 1990, *AJ*, 100, 32
 Böhringer H. et al., 2007, *A&A*, 469, 363
 Clarke T. E., Blanton E. L., Sarazin C. L., Anderson L. D., Gopal-Krishna, Douglass E. M., Kassim N. E., 2009, *ApJ*, 697, 1481

- Croston J. H. et al., 2008, *A&A*, 487, 431
 Ettori S., Brighenti F., 2008, *MNRAS*, 387, 631
 Evrard A. E., Metzler C. A., Navarro J. F., 1996, *ApJ*, 469, 494
 Fabian A. C., Sanders J. S., Taylor G. B., Allen S. W., Crawford C. S., Johnstone R. M., Iwasawa K., 2006, *MNRAS*, 366, 417
 Fabricant D., Lecar M., Gorenstein P., 1980, *ApJ*, 241, 552
 Finoguenov A., Henriksen M. J., Miniati F., Briel U. G., Jones C., 2006, *ApJ*, 643, 790
 Hernquist L., 1990, *ApJ*, 356, 359
 Ikebe Y., Reiprich T. H., Böhringer H., Tanaka Y., Kitayama T., 2002, *A&A*, 383, 773
 Lau E. T., Kravtsov A. V., Nagai D., 2009, *ApJ*, 705, 1129
 Lloyd-Davies E. J., Ponman T. J., Canon D. B., 2000, *MNRAS*, 315, 689
 Mazzotta P., Edge A. C., Markevitch M., 2003, *ApJ*, 596, 190
 Mohr J. J., Mathieson B., Evrard A. E., 1999, *ApJ*, 517, 627
 Nagai D., Vikhlinin A., Kravtsov A. V., 2007, *ApJ*, 655, 98
 Navarro J. F., Frenk C. S., White S. D. M., 1995, *MNRAS*, 275, 720
 Owers M. S., Couch W. J., Nulsen P. E. J., 2009, *ApJ*, 693, 901
 Piffaretti R., Valdarnini R., 2008, *A&A*, 491, 71
 Press W. H., Schechter P., 1974, *ApJ*, 187, 425
 Rasia E. et al., 2006, *MNRAS*, 369, 2013
 Richard J. et al., 2009, *MNRAS*, submitted
 Russell H. R., Sanders J. S., Fabian A. C., 2008, *MNRAS*, 390, 1207
 Sakelliou I., Ponman T. J., 2004, *MNRAS*, 351, 1439
 Sanderson A. J. R., Ponman T. J., O'Sullivan E., 2006, *MNRAS*, 372, 1496
 Sanderson A. J. R., O'Sullivan E., Ponman T. J., 2009a, *MNRAS*, 395, 764 (SOP09)
 Sanderson A. J. R., Edge A. C., Smith G. P., 2009b, *MNRAS*, 398, 1698
 Sarkar D., 2008, *Lattice: Multivariate Data Visualization with R*. Springer, Berlin
 Schmidt R. W., Allen S. W., 2007, *MNRAS*, 379, 209
 Vikhlinin A., Forman W., Jones C., 1999, *ApJ*, 525, 47
 Vikhlinin A., Kravtsov A., Forman W., Jones C., Markevitch M., Murray S. S., Van Speybroeck L., 2006, *ApJ*, 640, 691
 Vikhlinin A., Burenin R., Forman W. R., Jones C., Hornstrup A., Murray S. S., Quintana H., 2007, in Böhringer H., Pratt G. W., Finoguenov A., Schuecker P., eds, *Heating versus Cooling in Galaxies and Clusters of Galaxies*. Springer, Berlin, p. 48
 Voigt L. M., Fabian A. C., 2006, *MNRAS*, 368, 518
 Voit G. M., 2005, *Rev. Modern Phys.*, 77, 207
 Wegman E. J., 1990, *J. American Statistical Association*, 85, 664

APPENDIX A: ESTIMATING REAL VARIANCE

Consider some data d_i , with statistical errors σ_i and a set of estimates \hat{d}_i for these values, derived from a model. The deviations of d_i from \hat{d}_i consist of two parts: a statistical scatter, n_i , which is Gaussian distributed with zero mean and standard deviation σ_i , and a systematic offset, s_i , which we are interested in quantifying. Now

$$d_i = \hat{d}_i + n_i + s_i, \quad (\text{A1})$$

and we require an estimate of the fractional systematic deviation, s/\hat{d} , allowing for the possibility that it may be zero, i.e. the fluctuations of d_i about \hat{d}_i are entirely due to the measurement errors. It follows that

$$\begin{aligned} \langle (d_i - \hat{d}_i)^2 \rangle &= \langle (n_i + s_i)^2 \rangle = \langle n_i^2 + s_i^2 + 2n_i s_i \rangle \\ &= \langle n_i^2 \rangle + \langle s_i^2 \rangle = \sigma_i^2 + \langle s_i^2 \rangle, \end{aligned}$$

since $n_i s_i \rightarrow 0$ if the measurement errors have zero mean and are uncorrelated with s_i . So, our best estimate of s_i^2 is

$$\begin{aligned} \hat{s}_i^2 &= (d_i - \hat{d}_i)^2 - \sigma_i^2 \quad \text{for } \hat{s}_i^2 > 0, \\ \hat{s}_i^2 &= 0 \quad \text{for } \hat{s}_i^2 < 0. \end{aligned} \quad (\text{A2})$$

¹ <http://www.r-project.org>

We can estimate s/\hat{d} using

$$\left\langle \frac{s}{\hat{d}} \right\rangle = \frac{1}{n} \sum_{i=1}^n \left\langle \frac{s_i}{\hat{d}_i} \right\rangle = \frac{1}{n} \sum_{i=1}^n \frac{\langle s_i \rangle}{\hat{d}_i}$$

and insert the root mean square estimate for $\langle s_i \rangle$. Therefore our estimate of s/\hat{d} , the fractional non-statistical deviation, is given

by

$$f = \frac{1}{n} \sum_{i=1}^n \frac{\sqrt{\hat{s}_i^2}}{\hat{d}_i}. \quad (\text{A3})$$

This paper has been typeset from a $\text{\TeX}/\text{\LaTeX}$ file prepared by the author.